Applied Surface Science 567 (2021) 150882

Contents lists available at ScienceDirect

Applied Surface Science

journal homepage: www.elsevier.com/locate/apsusc

Full Length Article

DFT approaches unraveling the surface and morphological properties of $MnMoO_4$

Luis Henrique da Silveira Lacerda *, Miguel A. San-Miguel

State University of Campinas, Campinas, São Paulo, Brazil

ARTICLE INFO

Keywords:
Electronic structure
Surfaces
Photocatalysis
Antiviral and bactericide
Morphology
Magnetism

ABSTRACT

The $MnMoO_4$ is an environment-friendly semiconductor material with exciting properties and low cost to obtain highly employed supercapacitors. In this work, the α-$MnMoO_4$ phase was investigated by a careful DFT approach providing a detailed description of the electronic, optical, structural, magnetic, and photocatalytic properties of the surfaces. The results provide interesting insights on surface properties at the molecular level and point out novel applications for the evaluated materials, such as the treatment of water effluents or clean energy obtainment from water splitting. The available morphologies for $MnMoO_4$ were also investigated, enabling the tuning of material properties according to crystalline morphology.

1. Introduction

To maintain the fast technological advance experienced in our modern society, the development of new materials that attends to some specific features is mandatory [1,2]. Thus, the interest in novel environment-friendly materials with exciting properties and low fabrication costs increases drastically [3,4]. Among the limited number of candidates that meeting such conditions stands out the manganese molybdate ($MnMoO_4$), which is a semiconductor material extensively employed as a supercapacitor in the development of all kind of portable devices, electric/hybrid vehicles components, industrial power, instant switches, backup power sources, varied start engines, energy management, and others [1]. The supercapacitors represent the best power source today due to high power density, fast charging, low maintenance rate, high specific capacitance, and long lifespan (high number of operating cycles).

The relevance of manganese molybdate is also favored by the abundance in the Earth and outstanding structural (mechanic/thermal) stability [5]. Besides the previously mentioned supercapacitors developing, the $MnMoO_4$ material is also used in catalysts, optical and magnetic devices, and electrochemistry [6]. In summary, this material can be observed in three different polymorphs: α, β, and ω. The α-$MnMoO_4$ presents a C2/m space group where the Mn species occupies octahedral sites, and Mo atoms are surrounded by four O atoms, forming low-distorted tetrahedral [7–9]. This is the most stable phase of $MnMoO_4$, exhibiting remarkable stability under room conditions [10]. The β-$MnMoO_4$ exists in a wolframite structure (P2/c space group) where Mn and Mo atoms are octahedrally-coordinated sites. Consequently, in this polymorph, the Mn and Mo sites occupy 25 % of the interstitial positions of the distorted polyhedral close packing [11,12]. In turn, the ω-$MnMoO_4$ presents a $CoMnO_4$ structure where Mn and Mo atoms occupying octahedral and tetrahedral sites; differently from the α phase, the Mo polyhedra has a high distortion degree [12].

Due to the high interest in $MnMoO_4$ materials, several scientific studies were reported in literature focusing on the improvement of properties [13,14], fabrication of heterostructures [15,16], controlled synthesis routes to the obtainment of different morphologies [17,18], and device performance evaluation [19,20]. Although several manuscripts report morphological results for $MnMoO_4$, some experimental works present nanoparticles without well-defined crystal shapes showing properties evaluation [5,18]. Therefore, to the best of our knowledge, there is no detailed and broad investigation of the morphological features of $MnMoO_4$ and its relationship to observed properties.

In this work, the α-$MnMoO_4$ phase was investigated, presenting an in-depth DFT investigation of electronic, optical, structural, magnetic, and photocatalytic properties of surfaces predicting the potential applications for each available morphology. The obtained results provide interesting insights on surface properties at the molecular level and point out novel applications for the evaluated materials, such as the treatment of water effluents or production of atomic hydrogen from homolytic cleavage of water molecule aiming at renewable energy

* Corresponding author.
E-mail address: lhslacerda1@gmail.com (L.H.S. Lacerda).

https://doi.org/10.1016/j.apsusc.2021.150882
Received 30 May 2021; Received in revised form 27 July 2021; Accepted 6 August 2021
Available online 10 August 2021

resources and pollutants degradation.

2. Computational details

This manuscript presents DFT simulations to investigate the surface and morphological features of the α-$MnMoO_4$ material in the C2/m space group being the models constructed according to reported crystallographic data [21,22]. From the optimized bulk structure, the surface models were cut out along different crystalline directions parallel to specific *hkl* planes selected according to the prominent peaks observed on XRD results [21,22]. Thus, the low-index (220), (−112), (021), (112), (–222), (201), and (−202) surfaces were evaluated by stoichiometric models obtained from different slab stacking and compared in terms of surface energy. All possible stoichiometric slab stacking were tested for each surface, and the model with minor energy was chosen. In particular, all surface cuts investigated in this work result in polar surfaces since they present significant macroscopic dipole moment (μ_Z) [23]. The main reason behind this is that all possible stoichiometric surface models for each direction possess a high macroscopic dipole. Consequently, it is not possible to create non-polar surface models for the selected surface directions using our methodology because modeling non-defective and stoichiometric surfaces leads to polar surface cuts. Non-polar surfaces could be obtained by introducing surface defects, modeling non-stoichiometric models, adsorption of molecules on the surface, or reconstruction processes [24–27]. However, these kinds of approaches are far from the scope of this work.

Table 1 shows detailed information about surface models, summarizing the surface classification based on μ_Z value, the number of layers, surface thickness, and atomic composition. Surface models are shown in Fig. 1.

To adequately reproduce the surface effects experimentally reported, a slab growth was performed for all surfaces. Thus, a widely employed methodology consists of the growth of the surface models until convergence of surface energy values is achieved. This simple strategy does not require chemical adsorption or surface reconstruction to cancel the macroscopic dipole [26,28]. Firstly, the unrelaxed cleavage energy ($\gamma^{unrelax}$) was calculated from two complementary terminations using Equation (1). An unrelaxed surface termination is composed of the up (T_U) and down (T_D) terminations. $E_{slab}^{unrelax}$ and E_{bulk} refer to the total energies for the unrelaxed model and the bulk unit, respectively, n is the number of bulk units, and A is the surface area.

$$\gamma^{unrelax} = \frac{(\boldsymbol{E}_{slab}^{unrelax} - \boldsymbol{nE}_{bulk})}{2\boldsymbol{A}} \quad (1)$$

Next, the relaxation of each termination (T_U and T_D) was separately performed to obtain a surface model in which both terminations were optimized. The surface energy (γ) for relaxed models is computed by Equation (2). The scientific explanation for surface relaxation comes from structural modifications on the surface region to increase surface stability. It is essential to highlight that the applied methodology considers the internal polarization raised within the surface and its influence on surface energy and properties. The increase of surface thickness is also responsible for the minimization of the macroscopic dipole in polar surfaces. Table 1 contains the thickness of the converged models for each surface direction.

$$\gamma = \frac{(\boldsymbol{E}_{slab}^{relax} - \boldsymbol{nE}_{bulk})}{2\boldsymbol{A}} \quad (2)$$

Based on the calculated cleavage energies, it is possible to describe the energy cost to create a specific surface cut considering the breakage of chemical bonds and changes in the coordination numbers of cations sites on the surface. The methodology employed in this work is very representative and already successfully predicted the surface properties of several materials [29–37].

The magnetic features of the surface models were studied using the Ising Model. This method is required since Heisenberg hamiltonian, which defines the unpaired electrons, is not considered by *in silico* approaches. The Ising model represents a powerful tool to study magnetic solid-state materials [30–32,38–43]; however, this method can be employed only for highly periodic systems (such as the bulk phase), being impossible to fully apply it on surface investigations due to the modified coordination of magnetic sites in the surface. Therefore, it is not possible to determine the magnetic coupling constant (J) values for surfaces. Otherwise, using Equation (3) is possible to access the magnetic ground state of each surface by the energy difference (ΔE_T) between different magnetic states [35,36,38–40]. A positive value for ΔE_T indicates a ferromagnetic (FM) ground state; meanwhile, a negative value suggests an antiferromagnetic (AFM) or ferrimagnetic (FeM) ground state. To correctly reproduce the magnetic ground state, all possible magnetic orderings were evaluated for all surface directions.

$$\Delta E_T = E_{T_{AFM}} - E_{T_{FM}} \quad (3)$$

In particular, the quantum package used in this work employs a collinear method to elucidate the magnetic ordering describing the unpaired electrons as symmetrically distributed along the three spatial coordinates (x, y, and z). Further, the spin–orbit coupling (SOC) was neglected because spin symmetry is decreased/removed from the coupling effect; it is possible in complex oxide structures because collective spin ordering is determined from the Pauli rule, intrinsically associated with a crystalline structure. Different works [32,33,36,44,45] reported the efficiency of this approach, demonstrating agreement with experimental results.

Finally, based on surface investigation allied to Wulff construction, a large set of available morphologies for α-$MnMoO_4$ was predicted.

DFT-based calculations using B3LYP [46–49] hybrid functional as implemented in CRYSTAL17 [50,51] were carried out. Mn, Mo, and O atoms described by 86-411d41G [52], HAYWSC-311(d31)G [53], and 86-4111(41D)G [54] Gaussian basis sets, respectively. All calculations were performed in vacuum and 0 K. The energy self-consistent field (SCF) criteria convergence was 10^{-8}; the Mohnkhorst-Pack method [55,56] for k points sampling was set to 8 × 8 × 8, and the Coulomb and Hartree-Fock integrals defined as 10^{-8} and 10^{-16}.

Table 1
Features of low index surfaces of α-$MnMoO_4$ material.

	Layers composition in each minimal unit	Type	Thickness	
			Layers	Å
(220)	O_2—Mn—O_2—Mn—O_2—Mo_2—O_4—Mo_2—O_2—Mn—O_2—Mn—O_2	Polar	72	19.09
(–222)	O_3—Mn—O—Mn—O—Mo_2—O_6—Mo_2—O—Mn—O—Mn—O_3	Polar	72	14.81
(112)	O_4—Mo—O_2—Mn—O—Mo—Mn—O_2—Mn—Mo—O—Mn—O_2—Mo—O_4	Polar	72	8.06
(−202)	O_2 –Mn—Mo—O_6—Mn_2—Mo_2—O_6—Mo—Mn—O_2	Polar	45	9.43
(−112)	O_2—Mn—Mo—O_6—Mo—Mn_2—Mo—O_6—Mo—Mn—O_2	Polar	72	9.12
(021)	O—Mn_2—O_5—Mo—O—Mo—O—Mo—O_2—Mo—O_5—Mn_2 - O	Polar	66	11.27
(201)	O_3—Mn_2—O_3—Mn—O_5—Mo_4—O_5—Mn	Polar	48	9.74

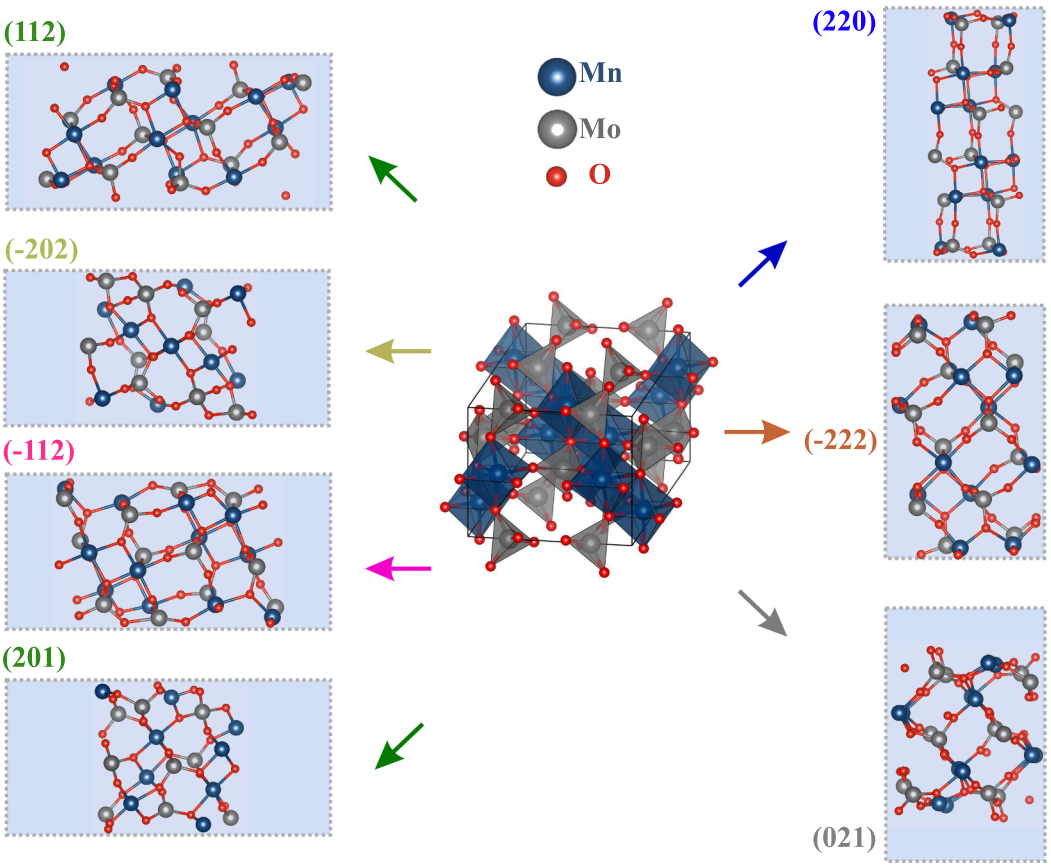

Fig. 1. Side view of the fully-relaxed surface models for α-$MnMoO_4$.

3. Results and discussion

3.1. Surface properties

3.1.1. Surface stability and structural features

The surface models for the C2/m phase of $MnMoO_4$ were constructed and evaluated according to previous computational details. (Table 2) presents the results for the cleavage energy ($\gamma^{unrelax}$), the surface energy (γ), the atom composition of both up and down terminations (T_U and T_D) for each surface, and the contribution of each termination to energy minimization. Moreover, Table 3 shows the coordination number of Mn and Mo cations and the density of defects (oxygen vacancies) in the surface.

In the α-$MnMoO_4$ structure, two different six-fold Mn sites and two different four-fold Mo sites are observed. The main difference between both sites is the distortion degree, which indicates how far the cation is displaced from the central position of the polyhedra. In summary, the Mo cation is slightly dislocated from the central position of the tetrahedral. In contrast, the Mn cations have a significant delocalization, presenting the highest distortion degree in the bulk structure. For the investigated $MnMoO_4$ surfaces, the surface energy increases following: (220) < (–222) < (112) < (−202) < (−112) < (021) < (201). The different surface energy values can be attached to some surface features, such as symmetrical terminations ($T_U = T_D$), the density of defects in each termination, and its atom composition. Thus, the most stable surface occurs along the (220) direction, being observed a symmetric O-

Table 2
Calculated values for calculated cleavage ($\gamma^{unrelax}$) and surface energy (γ), T_U and T_D contribution to energy minimization (%) and atom composition of both upper and down terminations (T_U and T_D). Energy values in J/m^2.

Surface	$\gamma^{unrelax}$	γ	T_U (%)	T_D (%)	Termination	
(220)	0.357	0.237	50.00	50.00	$T_U = T_D$	O—O—Mn—O
(–222)	0.987	0.551	50.01	49.99	$T_U = T_D$	O—O—O—Mn—O
(112)	1.431	0.833	39.16	60.84	T_U	O—O—O—O—Mo
					T_D	Mo—O—O—O—O
(−202)	1.838	0.998	53.17	46.83	T_U	O—O—Mo—Mn
					T_D	Mo—Mn—O—O
(−112)	2.288	1.069	62.03	37.97	T_U	O—O—Mn—Mo
					T_D	Mo—Mn—O—O
(021)	2.006	1.112	49.94	50.06	$T_U = T_D$	O—Mn—Mn—O
(201)	2.896	2.076	66.12	33.88	T_U	O—O—O—Mn
					T_D	O—O—O—Mn

Table 3
The coordination number for Mn and O atoms and the number of oxygen vacancies (V_O^X) on the two different upper and down terminations (T_U and T_D) for low index surfaces. The number of defects was calculated regarding the coordination of Mn and Mo cations within the bulk structure, i.e., [MnO_6] and [MoO_4] clusters.

Surface		Defects		
		Coordination number		V_O^X
		Mn	Mo	
(220)	$T_U = T_D$	5	–	1
(–222)	$T_U = T_D$	4	–	2
(112)	T_U	–	4	–
	T_D	–	4	–
(−202)	T_U	3	3	4
	T_D	3	2	5
(−112)	T_U	4	3	3
	T_D	4	3	3
(021)	$T_U = T_D$	3	–	3
(201)	T_U	3	–	3
	T_D	3	–	3

terminated surface with a low number of vacancies on both terminations. Following the increasing energy ordering, the (–222) surface is also a symmetric O-terminated surface but presents a high number of vacancies in T_U and T_D. In particular, the (112) direction is a symmetric O-terminated surface where both terminations possess the same chemical composition but different features for Mo sites. As presented in Table 4, the difference between both sites lies in bond lengths and, consequently, different distortion degrees for Mo clusters in T_U and T_D. This particular structural behavior yields higher γ values regarding (220) and (–222) surfaces, even in the absence of defects. For (−202) surface, different T_U and T_D terminations are observed. The T_U termination has exposed Mn cations while the T_D is O-terminated; both terminations exhibit a high density of defects since miss-coordinated [MnO] and [MoO] clusters are observed. The other surfaces are Mn-terminated ((−112) and (201)) or O-terminated ((021)) surfaces with a high number of vacancies around Mn and Mo sites. The Fig. 2 presents the clusters coordinations for all evaluated surfaces.

In terms of [MnO] and [MoO] cluster distortion degree, it is essential to highlight the specific octahedra exhibited in each surface. As previously mentioned, the bulk form presents distorted [MnO_6] and [MoO_4] clusters where the cations are significantly dislocated from the central position of the polyhedral. In the investigated surfaces, besides changes in Mn and Mo coordination numbers, the cations are profoundly dislocated from the central position of the polyhedral. This delocalization is mainly evidenced in Mo and Mn sites occupying the facets of polyhedra, being this type of cluster found in all investigated surfaces, except by the (220) direction. The existence of this kind of cluster can be connected to the photoluminescent behavior of solid-state materials [34,57–60].

In summary, the results indicate that a high number of vacancies is related to high surface energy, as previously reported [31,35,61]. Such influence is caused by the number of Mn—O and Mo—O bonds that should break to create a slab cut. Consequently, the number of dangling bonds represents the number of oxygen vacancies formed. However, the results also indicate that symmetric cuts (surface cuts with equal terminations) present minor energy due to a minor macroscopic dipole moment observed

Other essential comments lie on surface energy contribution to the energy minimization depicted in Table 2. This value indicates how much a termination is responsible for the surface energy minimization (γ) after structural relaxation. From such contribution, it is possible to predict the most stable termination and most likely to be obtained experimentally. As observed, the (220), (–222), and (021) are perfectly symmetric surfaces where both terminations are equal and have the same contribution to energy minimization. In the (112) surface, both terminations possess the same chemical composition; however, different features for Mo sites were observed. As previously mentioned, the difference between the cation sites in the up and down terminations comes from particular bond lengths and distortion degrees. The difference between both terminations justifies the different contributions to surface energy minimization (Table 2) and indicates the T_D as the most stable termination. The same behavior is observed for the (−112) surface, being the T_U the most favorable termination. The particular features of cations sites for such surfaces are presented in Table 4. The distortion degree values were determined from Equation (4), which relates the bond length (d_i), the average bond distance (d_{ave}), and the cation coordination number (c_n). In these cases, the results suggest that the surface termination with more distorted clusters presents higher surface energy. Finally, the (−202) and (201) surfaces are not symmetric cuts and have different terminations, being the T_U termination the most favorable in both cases.

$$\Delta = \frac{1}{c_n}\sum_i \left\{ \frac{(d_i - d_{ave})^2}{d_{ave}} \right\} \quad (4)$$

The obtained results for surface structural features are in agreement with other surface investigations for solid-state materials [33,35–37]. In general, surface energy is dependent on the coordination number observed for each cation (directly related to the O vacancy number) and the atom composition of the terminations. Finally, the influence of the density of defects on surface energy is related to the number of Mn—O and Mo—O bonds that need to be broken to obtain a slab cut.

3.1.2. Magnetic properties

Once the structural properties were discussed, other important features of $MnMoO_4$ surfaces come from unpaired electrons on Mn cations within the surface, resulting in magnetic properties for the surface and bulk phase. Since there are four magnetic sites in the C2/m bulk of $MnMoO_4$, and, consequently, four magnetic sites per bulk unit, several magnetic models (representing all the possible magnetic states) should be considered to determine the magnetic ground state and its magnetic moment. In this work, besides the magnetic ground state, the local and overall magnetic moment (μ_B) were evaluated, and the results are presented in Table 5. The results obtained for the bulk are in agreement with reports by Ehrenberg *et al.* [62] and Ochsenbein *et al.* [8], while the magnetism for surfaces has not been reported yet.

The (220), (−112), and (021) surfaces present AFM ground states, while the (112), (−202), and (201) surfaces possess a FeM ground state. In particular, the (–222) presents an FM ordering. As expected, the overall μ_B for AFM is null, while the FeM and FM surfaces show a high overall μ_B. The local μ_B for Mn sites indicates a slight decrease of spin-charge on Mn sites observed on the surface terminations regarding the bulk sites. In particular, the analysis of local μ_B for (112) and (−202) indicates an increase of spin population on Mo cations, which are non-magnetic species. As Lewars [63] stated and also well-known in literature, the spin population should be greater than 10 % of that observed on the magnetic species. On the other hand, the μ_B value is considered spin contamination observed as an intrinsic aspect of DFT methodology and not a behavior that can be experimentally expected for the material. Thus, for such surfaces, the spin population is not expected in experimentally obtained surfaces. In turn, it is expected a spin population on Mo sites for both terminations on (−112) surfaces and T_D terminations of (−202) surfaces. The spin population of O atoms was also evaluated and suggested that a magnetic moment is experimentally expected only on T_U terminations for (201) surfaces.

The three-dimensional representation of spin densities (Fig. 3) around the atoms in the surface corroborates that the spin population occurs on O 2p orbitals and Mo 4d orbitals. The 3D spin densities

Table 4
Bond lengths (Å) and cluster distortion degree (Δ) for (112) and (−112) surfaces of α-$MnMoO_4$.

Surface	Cluster features												
		[MoO_x]					[MnO_x]						
		Bond lengths (Å)				Δ (10^{-4})	Bond lengths (Å)						Δ (10^{-4})
		O_1	O_2	O_3	O_4		O_1	O_2	O_3	O_4	O_5	O_6	
(112)	T_U	1.767	1.842	1.930	2.028	26.59	–	–	–	–	–	–	–
	T_D	1.768	1.776	1.849	1.864	5.53	–	–	–	–	–	–	–
(−112)	T_U	1.793	1.796	1.864	–	3.25	2.061	2.063	2.081	2.134	–	–	2.00
	T_D	1.782	1.793	1.843	–	2.16	2.043	2.064	2.081	2.115	–	–	16.12

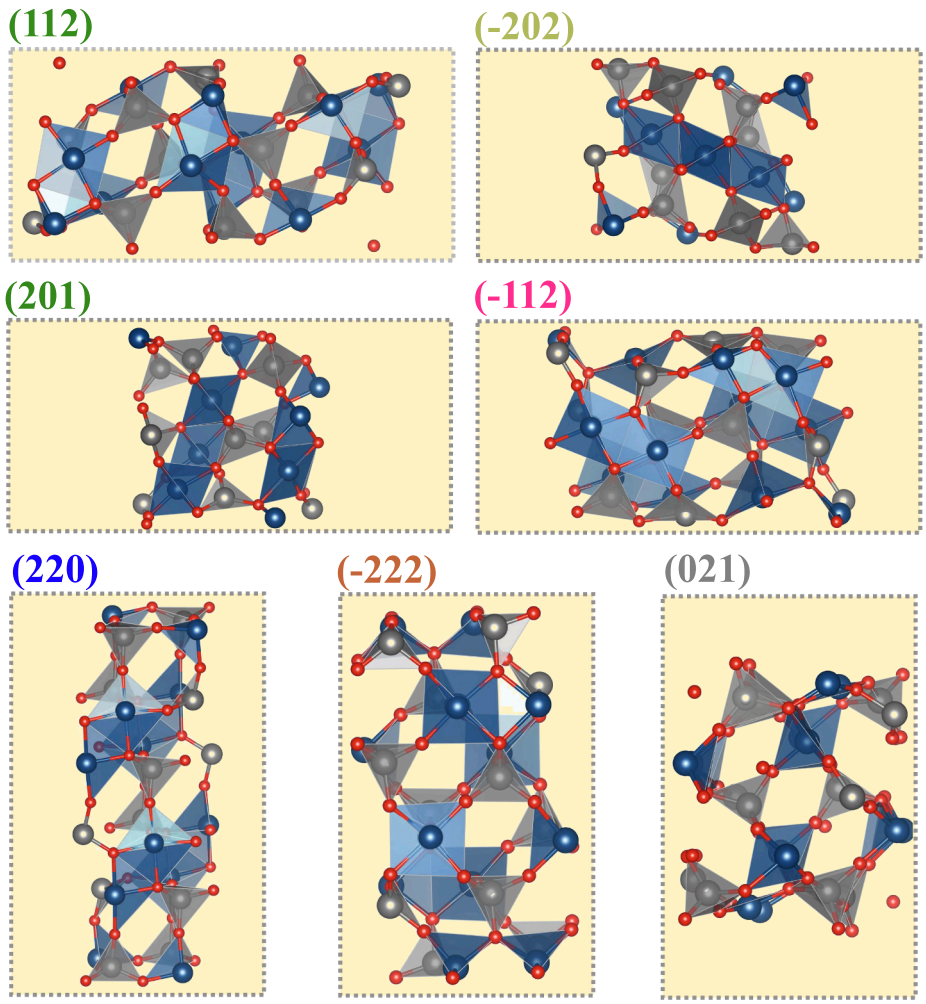

Fig. 2. [MnO] and [MoO] clusters in the investigated surfaces of $MnMoO_4$. The blue and gray polyhedral refers to Mn and Mo clusters.

Table 5
Magnetic ground states, overall μ_B, and local μ_B for Mn, Mo, and O species for surfaces. The oxygen atoms were labeled from 1 to 6 according to their respective distance from the magnetic cation.

Surface	Magnetic ground state	μ_B		μ_B (local)									
				Mn_1	Mn_2	Mo_1	Mo_2	O_1	O_2	O_3	O_4	O_5	O_6
Bulk	**AFM**	**0.0**		**4.747**	**4.745**	**0.047**	**0.048**	**0.015**	**0.014**	**0.011**	**0.08**	**0.06**	**0.04**
(220)	AFM	0.0	$T_U = T_D$	4.748	–	–	–	0.004	0.003	0.005	–	–	–
(–222)	FM	59.98	$T_U = T_D$	4.722	–	–	–	0.038	0.036	0.036	0.022	–	–
(112)	FeM	20.03	T_U	–	–	0.384	–	−0.181	0.027	0.020	−0.001	–	–
			T_D	–	–	−0.049	–	−0.036	−0.016	−0.014	0.001	–	–
(−202)	FeM	20.00	T_U	4.683	–	0.086	–	0.021	0.017	–	–	–	–
			T_D	4.674	–	0.903	–	0.002	0.002	–	–	–	–
(−112)	AFM	0.0	T_U	4.737	–	0.891	–	0.017	0.05	–	–	–	–
			T_D	−4.732	–	−0.864	–	−0.016	−0.010	–	–	–	–
(021)	AFM	0.0	$T_U = T_D$	4.681	4.661	–	–	0.014	0.011	–	–	–	–
(201)	FeM	5.99	T_U	4.668	–	–	–	0.862	0.699	0.184	–	–	–
			T_D	4.663	–	–	–	0.021	0.018	0.017	–	–	–

confirm our previous statement that no spin populations are observed for surfaces with spin charges minor than 0.4 |e| on O or Mo atoms. The density of defects can justify the existence of spin population on non-magnetic species on the surface, which comes from dangling bonds on Mn and Mo atoms spontaneously created when a surface outcrop occurs. The presence of vacancies is responsible for the degeneration of Mn and Mo d orbitals and O 2p orbitals, allowing the spin population in inter-metallic bonds (Mn—O—Mo). Similar behavior was observed on other complex oxides [31,32,35].

Finally, the magnetic evaluation provides some critical insights into the magnetism on complex oxides to understand the magnetism on α-$MnMoO_4$ surfaces and the influence of O vacancies on such properties. The existence of magnetism on the studied materials points out to promisor candidates developing actuators, magnetic sensors, spin-based devices (spintronic), magneto-capacitive devices, and other technological purposes.

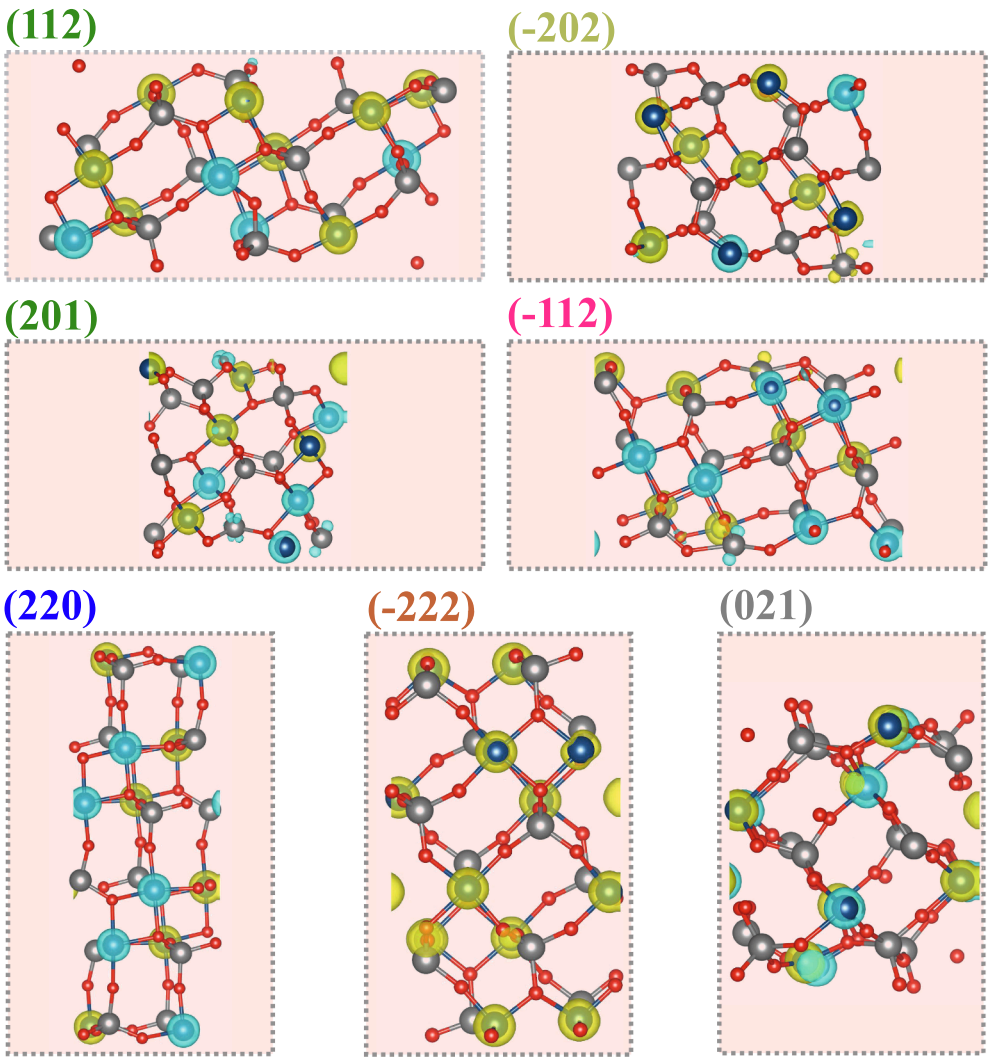

Fig. 3. 3D Spin Density for the investigated surfaces of α-$MnMoO_4$. The yellow and blue densities represent the alpha and beta electrons.

3.1.3. Electronic structure and properties

Once the structural and magnetic properties of α-$MnMoO_4$ surfaces were carefully depicted, the electronic structure of the investigated surfaces was discussed from the density of states (DOS) projection and band structures (BS), and the results presented in Fig. 4. The DOS analysis considers the atomic contribution in the valence band (VB) and conduction band (CB) energy regions; in turn, the BS considers the distribution of energy levels along the high symmetry points of the Brillouin zone (G, B, LD, and V) of the C2/m space group. Such high-symmetry points are among those observed for α-$MnMoO_4$ bulk structure and are the only ones that remain after the obtainment of the surfaces [64]. Both analyses were focused on the band gap region, taking into account the energy levels on the top of VB and the bottom of CB.

The DOS results show a relevant contribution of O atoms to the VB and CB; the Mn species contribute significantly to VB and CB while the Mo species contributes majorly on the top of VB and overall the CB. Therefore, the Mn, Mo, and O present the same contribution to the electronic structure for all surfaces. The BS indicates energy levels very close to each other on VB and CB for the (220) surface; as well as, in this surface, the energy levels are very dependent on high symmetry points of the Brillouin zone. The (−112) surface also presents a high dependency between energy levels and Brillouin zone points, but the energy difference between the VB or CB levels increases regarding the first mentioned surfaces. In particular, the (−202) and (112) surfaces present specific band structures since they present energy levels significantly spaced to each other in terms of energy as well as flat bands, corresponding to energy levels that are not influenced by the Brillouin zone symmetry points. The flat bands are observed as the bottom CB of the (021) surface, as the frontier energy levels of the α-spin channel of (112) surface; inner levels in VB of (–222), CB and VB for (201) direction, and the frontier energy levels for both spin channels of the (−202) surfaces. The flat band behavior can be attributed to O vacancies neighboring the Mn and Mo sites in the surface; as observed in the DOS projection, the flat bands in VB are composed of Mn while in CB are composed of O states. This behavior was previously observed for other complex magnetic oxides [33,35,36].

The application of the Fermi distribution [65,66] on calculated DOS makes possible the prediction of charge carrier concentration for solid-state materials, taking into account the influence of temperature on the number of holes ($h^{\bullet}$) and electrons (e^{-}). Thus, our results are in agreement with a reported experimental analysis and other theoretical calculations [67–71]. For semiconductors, the conduction process is majorly controlled by the predominant charge carrier. Thus, a higher number of holes refers to a p-type semiconductor where the conduction process is mainly related to holes; meanwhile, electrons are the predominant charge carrier involved in the conduction process for n-type semiconductors. Table 6 presents the results for charge carrier concentration at 300 K, 600 K, and 900 K for α-$MnMoO_4$ surfaces, suggesting an n-type conductivity for the bulk and (220), (021), the α-spin channel of (201), and β-spin channel of (–222), (112), and (−202) surfaces. The

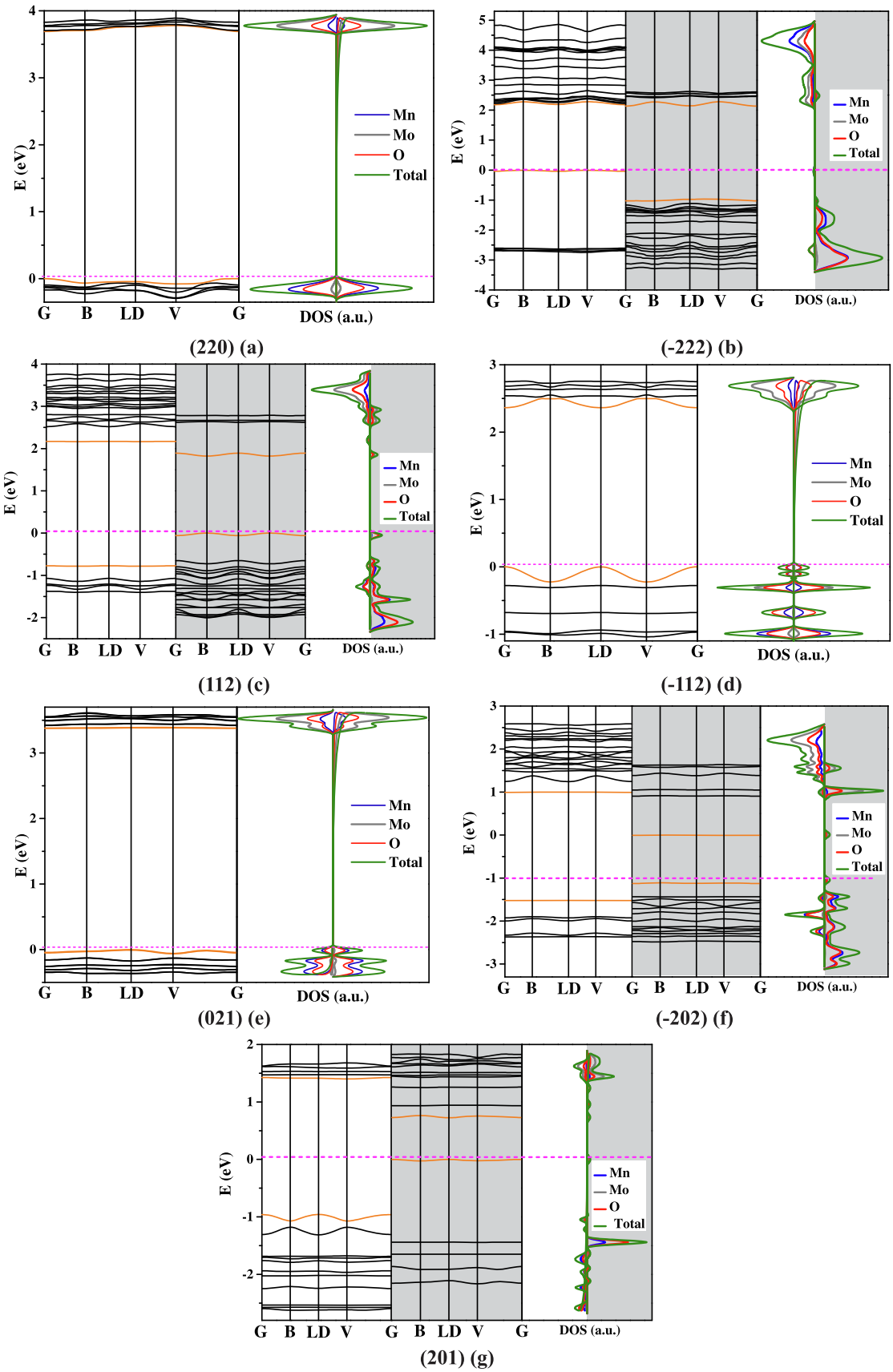

Fig. 4. Total Density of States (DOS) projection and Band Structures for investigated $MnMoO_4$ surfaces. The band structures analysis were performed along high symmetry points of the Brillouin Zone, which are G (0.0 0.0 0.0), B (0.5 0.0 0.0), LD (0.0 0.5 0.0), and V (0.5 0.5 0.0).

Table 6
Charge carrier density (cm^{-3}) at 300 K, 600 K, and 900 K obtained from Fermi distribution for bulk and surfaces of the $MnMoO_4$.

			Charge carrier density (cm^{-3})					
		Semiconductor type	300 K		600 K		900 K	
			holes	electrons	holes	electrons	holes	electrons
Bulk		n	$6.967 \cdot 10^{21}$	$7.229 \cdot 10^{21}$	$7.141 \cdot 10^{21}$	$7.409 \cdot 10^{21}$	$7.567 \cdot 10^{21}$	$7.851 \cdot 10^{21}$
(220)		n	$7.329 \cdot 10^{21}$	$7.748 \cdot 10^{21}$	$7.401 \cdot 10^{21}$	$7.824 \cdot 10^{21}$	$7.426 \cdot 10^{21}$	$7.898 \cdot 10^{21}$
(–222)	α	p	$2.325 \cdot 10^{23}$	$4.552 \cdot 10^{21}$	$2.330 \cdot 10^{23}$	$4.563 \cdot 10^{21}$	$2.332 \cdot 10^{23}$	$4.573 \cdot 10^{21}$
	β	n	$6.942 \cdot 10^{21}$	$2.024 \cdot 10^{23}$	$6.959 \cdot 10^{21}$	$2.029 \cdot 10^{23}$	$6.965 \cdot 10^{23}$	$2.033 \cdot 10^{23}$
(112)	α	p	$4.632 \cdot 10^{22}$	$7.295 \cdot 10^{21}$	$4.715 \cdot 10^{22}$	$7.425 \cdot 10^{21}$	$4.743 \cdot 10^{22}$	$7.553 \cdot 10^{21}$
	β	n	$6.081 \cdot 10^{21}$	$4.035 \cdot 10^{22}$	$6.190 \cdot 10^{21}$	$4.107 \cdot 10^{22}$	$6.227 \cdot 10^{21}$	$4.178 \cdot 10^{22}$
(−202)	α	p	$3.019 \cdot 10^{22}$	$1.124 \cdot 10^{22}$	$3.046 \cdot 10^{22}$	$1.134 \cdot 10^{22}$	$3.055 \cdot 10^{22}$	$1.143 \cdot 10^{22}$
	β	n	$8.058 \cdot 10^{21}$	$3.619 \cdot 10^{22}$	$8.129 \cdot 10^{21}$	$3.651 \cdot 10^{22}$	$8.154 \cdot 10^{21}$	$3.683 \cdot 10^{22}$
(−112)		p	$4.333 \cdot 10^{21}$	$4.103 \cdot 10^{21}$	$4.350 \cdot 10^{21}$	$4.120 \cdot 10^{21}$	$4.356 \cdot 10^{21}$	$4.135 \cdot 10^{21}$
(021)		n	$4.896 \cdot 10^{21}$	$5.727 \cdot 10^{21}$	$4.920 \cdot 10^{21}$	$5.755 \cdot 10^{21}$	$4.927 \cdot 10^{21}$	$5.781 \cdot 10^{21}$
(201)	α	p	$1.367 \cdot 10^{22}$	$6.183 \cdot 10^{21}$	$1.381 \cdot 10^{22}$	$6.244 \cdot 10^{21}$	$1.385 \cdot 10^{22}$	$6.303 \cdot 10^{21}$
	β	n	$1.487 \cdot 10^{22}$	$1.589 \cdot 10^{22}$	$1.502 \cdot 10^{22}$	$1.605 \cdot 10^{22}$	$1.507 \cdot 10^{22}$	$1.620 \cdot 10^{22}$

same semiconductivity type was experimentally reported for bulk and surfaces, indicating the reliability of our results [72,73]. The other surfaces are p-type semiconductors, being this behavior also reported for α-$MnMoO_4$ materials obtained from high-temperature synthesis [73]. As evidenced by DOS analysis, the p-type semiconductivity rises from a major contribution of the O atoms in VB, promoting the accumulation of positive charges on the surface. The semiconductivity type investigation for surfaces is crucial to understand the primary chemical entity responsible for the electronic conduction.

Table 7 presents the band gap and charge carrier stability for all investigated α-$MnMoO_4$ surfaces enabling us to predict optical properties. The α-MnMoO4 surfaces show a typical semiconductor bandgap, except for the β-spin channels for (−202) and (201) surfaces, which exhibit a characteristically conductor band gap. Thereby, the results point out the investigated surfaces as potential candidates to develop electronic and optical devices. It is also worth noticing that our theoretical prediction for bandgap values agrees with experimental results for bulk and surfaces [73–77]. This agreement strongly demonstrates the reliability of our DFT results. Furthermore, the existence of such results already reported in the literature did not minimize our scientific contribution once the experimental results only present a measurement of α-$MnMoO_4$ properties instead of a broad description of properties and surface features as presented in our work.

Table 7
Band gap (eV), effective masses of charge carriers, and work function (ϕ, in eV) for $MnMoO_4$ surfaces.

		Band-gap (eV)	Effective mass			Workfunction ϕ (eV)
			m_{h^*}/m_o	m_{e^*}/m_o	m_{h^*}/m_{e^*}	
Bulk		3.670 (V – G)	17.592	43.524	2.474	-
(220)		3.690 (G – G)	50.579	58.536	1.157	6.205
(–222)	α	2.180 (B – G)	58.962	43.263	0.734	5.775
	β	3.160 (LD – G)	116.447	17.794	0.153	
(112)	α	2.818 (V – B)	262.045	153.284	0.581	5.805
	β	1.795 (V – B)	44.963	35.152	0.782	
(−202)	α	2.513 (LD – G)	1365.640	172.639	0.126	5.179
	β	0.903 (B – G)	244.553	95.253	0.389	
(−112)		2.375 (G – G)	0.351	0.731	2.079	5.322
(021)		3.387 (LD – G)	48.352	178.294	3.687	4.307
(201)	α	2.352 (LD – V)	20.447	163.389	7.991	4.448
	β	0.724 (LD – LD)	58.962	43.815	0.743	

Besides electronic and optical potential, the photocatalytic activity for the evaluated surfaces can be estimated from charge carriers stability (Table 7). The study of charge mobility (stability) is mandatory to determine the photocatalytic potential of a material and can be performed through the effective mass method [78–81]. Thus, the electron (m_{h^*}/m_o) and hole (m_{e^*}/m_o) effective masses are calculated from Equation (5) and Equation (6), where m* is the effective mass of the charge carrier, k is the wave vector, $\hbar$ is the reduced Planck constant, and ν is the transfer rate of electrons and holes photogenerated. From the ratio between effective masses of electrons (e^-) and holes ($h^\bullet$) (m_{h^*}/m_{e^*}) it is possible to determine the recombination rate of photogenerated electron-hole pairs. Usually, low rates (ratio values minor than 0.5 or higher than 1.5) are related to increased photocatalytic efficiency [82–85]. Before stating the potential candidates for photocatalytic-based applications, it is noteworthy that the desired material for this kind of application presents band gaps in the visible region of the electromagnetic spectrum (1.6 eV to 3.3 eV) [86]. Therefore, it is expected that the (−202), (−112), and (021) surfaces of α-$MnMoO_4$ possess fascinating properties for photocatalytic purposes, being strong alternatives to the development of photocatalysts. The high stability of charge carriers is also exciting for thermoelectric applications [87–90]. The reliability of the prediction of the photocatalytic potential by such methodology can be evidenced from the similarity of our theoretical results for (220) surfaces and experimentally obtained nanorods (majorly composed by this surface), since both approaches suggest a low photocatalytic potential for this material [7].

$$\nu = \hbar k / m^* \tag{5}$$

$$m^* = \hbar^2 \left(\frac{d^2 E}{dk^2} \right)^{-1} \tag{6}$$

Moreover, the work function (ϕ) for α-$MnMoO_4$ surfaces was computed as the difference between electrons in the infinite (E_∞) and the Fermi energy level (E_F) [91,92]. The work function represents the required energy to remove an electron from each materials surface [93]. The calculated ϕ values show that the lowest work function is observed for the (021) surface, while the (220) surface possesses the highest value. Therefore, it is expected that photogenerated electrons to be found preferentially in (021) surfaces which act as reductive centers throughout the morphologies. Otherwise, the (220) surface concentrates the holes, creating a promising oxidative center. The results yield a charge gradient throughout the crystal, promoting the migration of the hole (positive) and electron (negative) carriers to distinct exposed surfaces [94,95].

Finally, another critical analysis lies in the determination of valence

and conduction band edge potentials. While the band gap determines the interaction of materials surface with radiation, the band edge locations indicate the redox potentials of charge carriers during surface reactions [96,97]. Consequently, it is possible to predict what reactions can occur on the surface by comparing the surface band edges and the potential formation of different reactive oxygen species (ROS). In this work, the valence and conduction band edge potentials for α-$MnMoO_4$ were computed using the calculated Mulliken electronegativity (χ = 5.94 eV); the band edge potential values with respect to vacuum and the hydrogen electrode potential compose Fig. 5. The values were calculated from a well-known set of equations [98,99], and its efficiency is proven by a good agreement with experimental evidences [94,98,100]. The results indicate that VB edge potential values are more positive than the O_2/H_2O (1.23 V) potential for all surfaces and bulk; consequently, α-$MnMoO_4$ can oxidize H_2O molecules to produce O_2 or also to oxidize pollutants. In turn, the values for CB edge potential suggest that the bulk and (220) and (021) surfaces can reduce H^+ to H_2 (0 V). The surfaces with such ability are potential alternatives to the sustainable obtainment of energy from H_2 produced from water splitting [101–106].

Based on the CB and VB band edge potentials, it is also possible to predict the antiviral and bactericidal potential of semiconductor materials. This is a critical feature, mainly in recent days. Over the years, the human beings have faced several kinds of viral threads, such as SARS, Ebola Virus, H1N2 (2009 influenza), MERS, and SARs-CoV-2 [107,108]. The spread of these viruses occurs through person-to-person, contact with airborne droplets containing viruses, or indirectly by contact with contaminated surfaces or objects [109,110]. In particular, the SARs-CoV-2 virus, also known as COVID-19, has changed the world drastically in 2020, and its effects are still felt in 2021. Several antiviral agents that deactivate viruses by denaturing their proteins were largely employed to avoid contamination and stop the virus spread [111]. However, these compounds still no present the desired efficiency due to the surface protection time. In this context, solid-state materials stand out as potential alternatives to developing robust antiviral surfaces with long virus-deactivation time. Further, it is also expected that this kind of material presents high antibacterial effects. In summary, the antiviral and antibacterial potential of this kind of metals, semiconductors, and other solid-state materials is related to the photogeneration of ROS from ultraviolet or visible radiation absorption. The ROS can kill pathogens directly through oxidative damage to biological compounds or indirectly by non-oxidative paths such as autophagy or T-lymphocyte responses [111–118]. One of the essential features of photoinduced antiviral effects lies in a high concentration of ROS, which also guarantees a long-time antibacterial activity on materials surfaces to bleach even drug-resistant bacteria [115].

To the best of our knowledge, the antiviral and antibacterial properties of α-$MnMoO_4$ were not reported yet. Thereby, this work evaluates these features of α-$MnMoO_4$ surfaces, comparing the VB and CB edges values to the formation potential of $^{\bullet}O_2^-$, H^+/H_2, O_2/H_2O, singlet/dioxygen and $H_2O/^{\bullet}OH$ couple species. The reliability of this approach is corroborated by experimental and theoretical data reported by Li *et al.* [119] and He *et al.* [108]. Our results suggest that all investigated surfaces can interact with ultraviolet or visible radiation, creating at least one ROS type. Thus, a possible antiviral and antibacterial property is expected for α-$MnMoO_4$ surfaces, mainly (220), (–222), and (021) surfaces which can create all the mentioned ROS. In this context, it is noteworthy the possible antiviral and bactericidal potential of the α-$MnMoO_4$ (220) surfaces, which is the most stable and majorly observed surface in experimental results [1,3,4]. The results suggest the possibility of producing α-$MnMoO_4$-based masks, cloths, gloves, and other health devices with high antiviral and antibacterial potential. Furthermore, the development of inks and other protections for surfaces or objects represents a critical alternative to stop/minimize the spread of the virus in indoor environments.

3.2. Crystal morphology

In this section, the available crystal morphologies for α-$MnMoO_4$ were predicted using the Wulff model [120,121], employing the γ values for the main surfaces to obtain an ideal morphology. Other morphologies were then obtained by tuning the γ values of specific surfaces; this theoretical strategy allows to access different crystal shapes and compares with those morphologies experimentally obtained through different synthesis routes or conditions [122–124]. The contribution of each surface to the morphology is inversely proportional to its γ, then low γ values correspond to a high contribution to the crystal shape.

Fig. 6 presents a complete set of available morphologies for α-$MnMoO_4$ materials. The ideal morphology (0) is mainly composed of (220) surfaces allied to a significant contribution of (–222) surface. From this polymorph, a complete set of available morphologies was obtained, decreasing γ for (220) surfaces, resulting in the (1) and (1.1) morphologies, which were often reported by SEM images [1,3,4,6,10,125–128]. The (2) and (3) sets were obtained by tuning the (–222) and (112) surfaces being obtained balloons-like crystal shapes very similar to that reported by Zhang *et al.* [11], Lee *et al.* [19], Lei *et al.* [12] and Wang *et al.* [129]. The fourth set – (4) – was obtained from tuning more than one surface energy, resulting in several prismatic shapes; in this set stand out the (4) crystal shape that is very similar to the crystal shapes obtained in Ref. [76]. Likewise, the (5), (6), and (7) sets are composed of prismatic shapes with a significant contribution of (220) surface allied to a significant contribution of (−202), (−112), and (021) surfaces, respectively. From these sets, the (5.2) [17], (6.2)

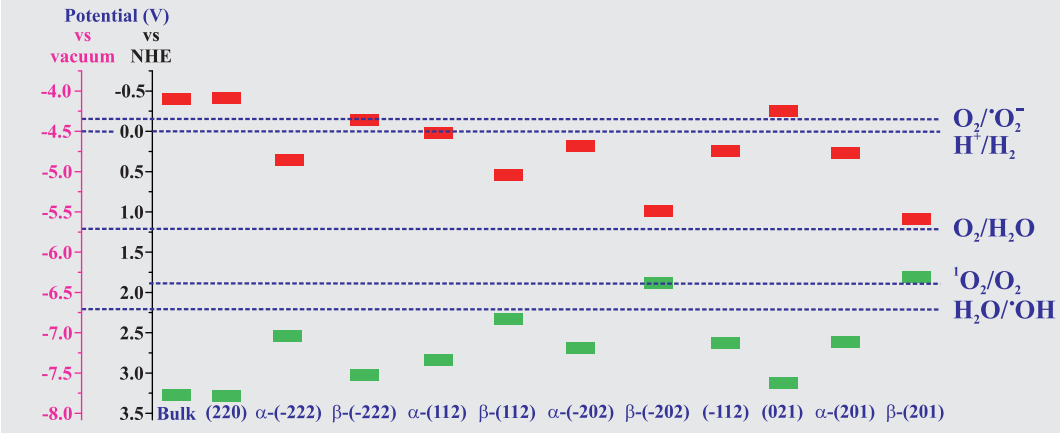

Fig. 5. Calculated valence (green) and conduction (red) band edge potential for bulk and surfaces of $MnMoO_4$ surfaces with respect to Hydrogen electrode potential (NHE) and vacuum.

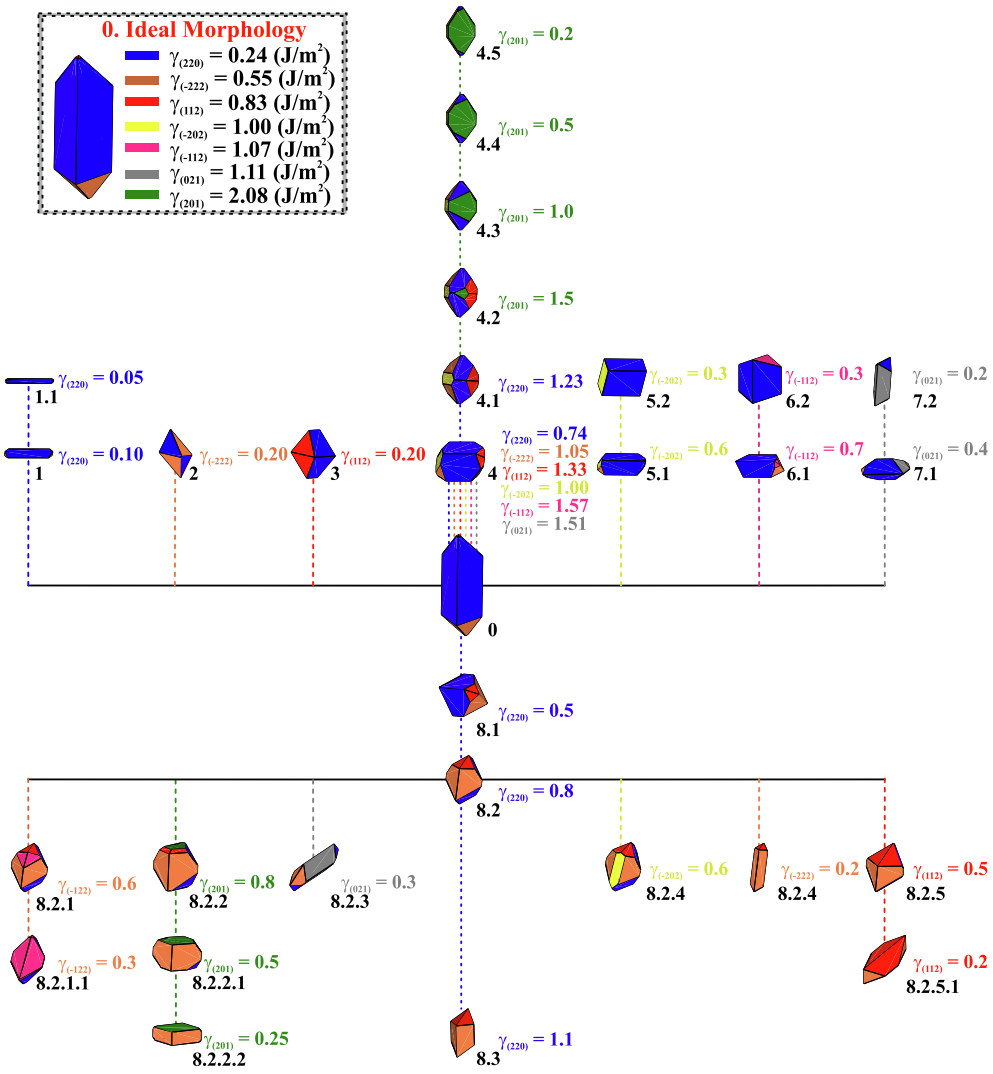

Fig. 6. Complete set of available morphologies for $MnMoO_4$ considering the (220), (–222), (112), (−202), (−112), (021), and (201) surfaces. The color of the dashed lines indicates which surface energy was tuned to reach each crystal shape, being the new energy value presented along the morphology. The surface energy (γ) values are in J/m^2.

[11], and (7.2) [130] are in agreement with experimental results. Finally, the (8) set contains plate-like (8.2.2.2), diamond-like (8.2.5, 8.2.5.1, and 8.3), and nanorods (8.2.3 and 8.2.4) shapes. In this set, the (8.2) [7,131], (8.2.2) [76], (8.2.2.2) [131], and (8.2.5.1) [12] crystal shapes are very similar to SEM results observed in the literature.

From these theoretical results, it is feasible to relate a predicted crystal morphology to its expected properties. In summary, the suitability of α-$MnMoO_4$ to be used in electronic, optical, magnetic, and photocatalytic devices or processes was evaluated. Electronic devices are typically developed by conductor or semiconductor materials, while optical devices require only semiconductor materials with a band gap ranging from 1.65 eV to 3.35 eV; this range refers to the visible range of the electromagnetic spectrum. Therefore, all predicted morphologies are potential alternatives for developing general electronic and optical devices due to band gap values. Meanwhile, crystal shapes with significant magnetization can be applied to the development of magnetic-based devices; in this scenario, the (3), (4), (4.1), (4.2), (5.2), (8.2.2), (8.2.4), (8.2.5), (8.2.5.1), (8.2.5.4), and (8.3) morphologies are potential candidates due to high magnetization in (1 1 2) and (−2 0 2) surfaces. In the case of the photocatalytic process, which characteristically requires good stability of charge carriers (as evaluated by charge carrier effective mass) allied to visible-range band gap and ability to reduce or oxidize H_2O molecules, the results indicate the morphologies with a significant contribution of (−2 0 2), (−1 1 2), and (0 2 1) surfaces. Thus, is expected a powerful photocatalytic potential for (4.1), (5.2), (6.2), (7.1), (7.2), (8.2.1), and (8.2.1.1) polymorphs. Similarly, the ability of the (0 2 1) surfaces to produce H_2 from H_2O reduction suggests the (7.1), (7.2), and (8.2.3) shapes as potential candidates for photocatalytic water splitting purposes. Thereby, the results evidence the high versatility of α-$MnMoO_4$ since one crystal shape is suitable for at least two different goals.

4. Conclusion

This manuscript reports a careful DFT/B3LYP investigation of surface properties and morphologies for the $MnMoO_4$ in the C2/m space group. The structural, magnetic, electronic, optical, and photocatalytic properties of the main surfaces were investigated. The main conclusions are summarized as follows.

(i) The stability of α-$MnMoO_4$ surfaces decreases in the order (2 2 0) > (–2 2 2) > (1 1 2) > (−2 0 2) > (−1 1 2) > (0 2 1) > (2 0 1). The different surface energies can be justified by density of defects (vacancies) in the surface, surface symmetric or non-symmetric terminations and chemical composition of surface termination;

(ii) The investigation of magnetic properties indicates an antiferromagnetic ground state for (220), (−112), (021), and (201) surfaces and a ferrimagnetic ground state for (112) and (−202) surfaces;
(iii) A high number of vacancies around the Mn and Mo sites creates a spin population on Mo sites for both terminations on (−112) surfaces and O atoms on T_D terminations of (−202) surfaces. Thus, local magnetic moments are observed in these non-magnetic sites;
(iv) The evaluation of the density of states indicates that, for all surfaces, O atoms present a relevant contribution to the VB and CB, Mn species contribute significantly to the formation of VB and CB. In contrast, the Mo species contributes majorly on the top of VB and overall of CB. The band structure also indicates the existence of flat bands for (021), (112), and (−202) surfaces, being this behavior raised from O vacancies neighboring the Mn and Mo sites in the surface;
(v) The evaluation of electronic and optical properties typically indicates conductor or semiconductor band gaps. The study of available states on valence and conduction bands suggests which charge carrier (electron or hole) is the primary responsible for the conduction process;
(vi) The stability of charge carriers, allied to suitable band gaps values, indicates a high photocatalytic potential for (−202), (−112), and (021) surfaces.
(vii) The valence and conduction band edge potential vs. NHE electrode indicates that bulk and surfaces of $MnMoO_4$ can oxidize H_2O molecules to produce O_2 or oxidize pollutants. The results also suggest that the bulk and (220) and (021) surfaces can reduce H^+ to H_2.
(viii) All investigated α-$MnMoO_4$ surfaces present a possible antiviral and bactericidal potential since they can produce at least one type of reactive oxygen species (ROS). The (220), (–222), and (021) surfaces stand out as the most promising alternatives due to their ability to produce five different ROS.
(ix) The morphological sets include both reported and novel crystalline shapes for α-$MnMoO_4$.
(x) The predicted morphologies for α-$MnMoO_4$ exhibit a high versatility since one crystal shape is suitable for at least two different technological purposes such as electronic, optical, magnetic, photocatalytic, or water splitting.

Finally, the prediction of a large set of crystal shapes to solid-state materials is critical to materials development and provides a valuable strategy to control its properties through morphology adaptation. Thus, this study is strongly indicated to guide experimental scientists focused on novel or improved applications of α-$MnMoO_4$.

CRediT authorship contribution statement

Luis Henrique da Silveira Lacerda: Conceptualization, Data curation, Formal analysis, Investigation, Methodology, Software, Visualization, Writing – original draft, Writing – review & editing. **Miguel A. San-Miguel:** Funding acquisition, Project administration, Supervision, Resources, Writing – review & editing.

Declaration of Competing Interest

The authors declare that they have no known competing financial interests or personal relationships that could have appeared to influence the work reported in this paper.

Acknowledgments

The authors acknowledge support from São Paulo Research Foundation (FAPESP) for grants 2013/07296-2, 2016/23891-6, 2017/26105-4, and 2020/03780-0 and the "Centro de Computação John David Rogers" (CCJDR-UNICAMP). The authors also acknowledge Professor. Dr. Sergio Ricardo de Lazaro (UEPG) for the computational facilities of Grupo de Simulação Química (GSQ).

Appendix A. Supplementary material

Supplementary data to this article can be found online at https://doi.org/10.1016/j.apsusc.2021.150882.

References

[1] J. Yesuraj, V. Elumalai, M. Bhagavathiachari, A.S. Samuel, E. Elaiyappillai, P. M. Johnson, A facile sonochemical assisted synthesis of α-MnMoO4/PANI nanocomposite electrode for supercapacitor applications, J. Electroanal. Chem. 797 (2017) 78–88.
[2] X. Mu, Y. Zhang, H. Wang, B. Huang, P. Sun, T. Chen, J. Zhou, E. Xie, Z. Zhang, A high energy density asymmetric supercapacitor from ultrathin manganese molybdate nanosheets, Electrochim. Acta 211 (2016) 217–224.
[3] C. Peng, L. Gao, S. Yang, J. Sun, A general precipitation strategy for large-scale synthesis of molybdate nanostructures, Chem. Commun. (2008) 5601–5603.
[4] B. Guan, W. Sun, Y. Wang, Carbon-Coated MnMoO4 Nanorod for High-Performance Lithium-Ion Batteries, Electrochim. Acta 190 (2016) 354–359.
[5] C. Sekar, R.K. Selvan, S.T. Senthilkumar, B. Senthilkumar, C. Sanjeeviraja, Combustion synthesis and characterization of spherical α-MnMoO4 nanoparticles, Powder Technol. 215–216 (2012) 98–103.
[6] T. Watcharatharapong, M. Minakshi Sundaram, S. Chakraborty, D. Li, G. M. Shafiullah, R.D. Aughterson, R. Ahuja, Effect of Transition Metal Cations on Stability Enhancement for Molybdate-Based Hybrid Supercapacitor, ACS Appl. Mater. Interfaces 9 (2017) 17977–17991.
[7] V.K.V.P. Srirapu, A. Kumar, N. Kumari, P. Srivastava, R.N. Singh, A comparative study of electrocatalytic performance of metal molybdates for the water oxidation, Int. J. Hydrogen Energy 43 (2018) 16543–16555.
[8] S.T. Ochsenbein, G. Chaboussant, A. Sieber, H.U. Güdel, S. Janssen, A. Furrer, J. P. Attfield, Magnetic cluster excitations in the antiferromagnetic phase of α-$MnMoO_4$, Phys. Rev. B 68 (2003), 092410.
[9] S.C. Abrahams, J.M. Reddy, Crystal Structure of the Transition-Metal Molybdates. I. Paramagnetic Alpha-MnMoO4, J. Chem. Phys. 43 (1965) 2533–2543.
[10] H. Cao, N. Wu, Y. Liu, S. Wang, W. Du, J. Liu, Facile synthesis of rod-like manganese molybdate crystallines with two-dimentional nanoflakes for supercapacitor application, Electrochim. Acta 225 (2017) 605–613.
[11] C. Zhang, D. Wu, L. Shi, Y. Zhu, D. Xiong, S. Xu, R. Huang, R. Qi, W. Zhang, L. Wang, P.K. Chu, Manganese molybdate nanoflakes on silicon microchannel plates as novel nano energetic material, Roy. Soc. Open Sci. 4 (2017), 171229.
[12] S. Lei, K. Tang, Q. Liu, Z. Fang, Q. Yang, H. Zheng, Preparation of manganese molybdate rods and hollow olive-like spheres, J. Mater. Sci. 41 (2006) 4737–4743.
[13] V.K.V.P. Srirapu, M. Kumar, R. Awasthi, R.N. Singh, A.S.K. Sinha, Manganese molybdate and its Fe-substituted products as new efficient electrocatalysts for oxygen evolution in alkaline solutions, Int. J. Hydrogen Energy 38 (2013) 13587–13595.
[14] Y. Cao, W. Li, K. Xu, Y. Zhang, T. Ji, R. Zou, J. Yang, Z. Qin, J. Hu, MnMoO4·4H2O nanoplates grown on a Ni foam substrate for excellent electrochemical properties, J. Mater. Chem. A 2 (2014) 20723–20728.
[15] L.-Q. Mai, F. Yang, Y.-L. Zhao, X. Xu, L. Xu, Y.-Z. Luo, Hierarchical MnMoO4/CoMoO4 heterostructured nanowires with enhanced supercapacitor performance, Nat. Commun. 2 (2011) 381.
[16] X. Feng, Y. Huang, M. Chen, X. Chen, C. Li, S. Zhou, X. Gao, Self-assembly of 3D hierarchical MnMoO4/NiWO4 microspheres for high-performance supercapacitor, J. Alloy. Compd. 763 (2018) 801–807.
[17] D. Ghosh, S. Giri, M. Moniruzzaman, T. Basu, M. Mandal, C.K. Das, α MnMoO4/graphene hybrid composite: high energy density supercapacitor electrode material, Dalton Trans. 43 (2014) 11067–11076.
[18] M. Isacfranklin, B.J. Rani, G. Ravi, R. Yuvakkumar, S.I. Hong, D. Velauthapillai, B. Saravanakumar, Hydrothermal Method-Derived MnMoO4 Crystals: Effect of Cationic Surfactant on Microstructures and Electrochemical Properties, ChemistrySelect 5 (2020) 7728–7733.
[19] G.-H. Lee, S. Lee, J.-C. Kim, D.W. Kim, Y. Kang, D.-W. Kim, MnMoO4 Electrocatalysts for Superior Long-Life and High-Rate Lithium-Oxygen Batteries, 7 (2017) 1601741.
[20] L. Wen, Y. Sun, T. Zhang, Y. Bai, X. Li, X. Lyu, W. Cai, Y. Li, MnMoO4 nanosheet array: an efficient electrocatalyst for hydrogen evolution reaction with enhanced activity over a wide pH range, Nanotechnology 29 (2018), 335403.
[21] D.P. Dutta, A. Mathur, J. Ramkumar, A.K. Tyagi, Sorption of dyes and Cu(ii) ions from wastewater by sonochemically synthesized MnWO4 and MnMoO4 nanostructures, RSC Adv. 4 (2014) 37027–37035.
[22] K.K. Purushothaman, M. Cuba, G. Muralidharan, Supercapacitor behavior of α-MnMoO4 nanorods on different electrolytes, Mater. Res. Bull. 47 (2012) 3348–3351.
[23] P.W. Tasker, The stability of ionic crystal surfaces, J. Phys. C: Solid State Phys. 12 (1979) 4977–4984.

[24] J.-P. Jacobs, M.A.S. Miguel, L.J. Alvarez, Studies of LaAlO3 100 surfaces by molecular dynamics simulations, J. Mol. Struct. (Thoechem) 390 (1997) 193–198.
[25] J.-P. Jacobs, M.A.S. Miguel, J.E. Sánchez-Sánchez, L.J. Álvarez, On the origin of the reconstruction of LaAlO3 100 surfaces, Surf. Sci. 389 (1997) L1147–L1152.
[26] Y. Dai, Q. Gao, C. Cui, L. Yang, C. Li, X. Li, Role of ferroelectric/ferromagnetic layers on the ferroelectric properties of magnetoelectric composite films derived by chemical solution deposition, Mater. Res. Bull. 99 (2018) 424–428.
[27] J. Jin, H. Li, C. Chen, B. Zhang, L. Xu, B. Dong, H. Song, Q. Dai, Enhanced Performance of Perovskite Solar Cells with Zinc Chloride Additives, ACS Appl. Mater. Interfaces 9 (2017) 42875–42882.
[28] J.-Q. Dai, J.-W. Xu, J.-H. Zhu, Thermodynamic Stability of BiFeO3 (0001) Surfaces from ab Initio Theory, ACS Appl. Mater. Interfaces 9 (2017) 3168–3177.
[29] M.M. Teixeira, R.C. de Oliveira, M.C. Oliveira, R.A. Pontes Ribeiro, S.R. de Lazaro, M.S. Li, A.J. Chiquito, L. Gracia, J. Andrés, E. Longo, Computational Chemistry Meets Experiments for Explaining the Geometry, Electronic Structure, and Optical Properties of Ca10V6O25, Inorg. Chem. 57 (2018) 15489–15499.
[30] R.A.P. Ribeiro, S.R. de Lazaro, L. Gracia, E. Longo, J. Andrés, Theoretical approach for determining the relation between the morphology and surface magnetism of Co3O4, J. Magn. Magn. Mater. 453 (2018) 262–267.
[31] R.A.P. Ribeiro, J. Andrés, E. Longo, S.R. Lazaro, Magnetism and multiferroic properties at MnTiO3 surfaces: A DFT study, Appl. Surf. Sci. 452 (2018) 463–472.
[32] R.A.P. Ribeiro, E. Longo, J. Andrés, S.R. de Lazaro, A DFT investigation of the role of oxygen vacancies on the structural, electronic and magnetic properties of ATiO3 (A = Mn, Fe, Ni) multiferroic materials, PCCP 20 (2018) 28382–28392.
[33] R.A.P. Ribeiro, L.H.S. Lacerda, E. Longo, J. Andrés, S.R. de Lazaro, Towards enhancing the magnetic properties by morphology control of ATiO3 (A = Mn, Fe, Ni) multiferroic materials, J. Magn. Magn. Mater. 475 (2019) 544–549.
[34] M.C. Oliveira, R.A.P. Ribeiro, L. Gracia, S.R. de Lazaro, M. de Assis, M. Oliva, I.L. V. Rosa, M.F.d.C. Gurgel, E. Longo, J. Andrés, Experimental and theoretical study of the energetic, morphological, and photoluminescence properties of CaZrO3: Eu3+, CrystEngCommCrystEngComm 20 (2018) 5519–5530.
[35] L.H.d.S. Lacerda, S.R. de Lazaro, Theoretical investigation on the surface and morphological properties of lead nickelate multiferroics: vacancy dependency, J. Mater. Sci. 55 (2020) 6875–6890.
[36] L.H.d.S. Lacerda, S.R. de Lazaro, Surface and morphology investigation of FeCrO3 material in ilmenite-, corundum- and lithium niobate- polymorphs, Surf. Interfaces 22 (2021), 100837.
[37] A.F. Gouveia, L. Gracia, E. Longo, M.A. San-Miguel, J. Andrés, Modulating the properties of multifunctional semiconductors by means of morphology: Theory meets experiments, Comput. Mater. Sci. 188 (2021), 110217.
[38] R.A.P. Ribeiro, S.R. de Lazaro, S.A. Pianaro, Density Functional Theory applied to magnetic materials: Mn_3O_4 at different hybrid functionals, J. Magn. Magn. Mater. 391 (2015) 166–171.
[39] A. Chartier, P. D'Arco, R. Dovesi, V.R. Saunders, Ab initio Hartree-Fock investigation of the structural, electronic, and magnetic properties of Mn_3O_4, Phys. Rev. B 60 (1999) 14042–14048.
[40] X. Feng, N.M. Harrison, Magnetic coupling constants from a hybrid density functional with 35% Hartree-Fock exchange, Phys. Rev. B 70 (2004) 092402–092405.
[41] L.H.d.S. Lacerda, S.R. de Lazaro, A DFT investigation on magnetoelectric coupling in PbBO3 (B = V, Cr, Mn Co, and Cu) materials: The influence on multiferroic properties, J. Magn. Magn. Mater. 500 (2020) 166364–166374.
[42] L.H.d.S. Lacerda, R.A.P. Ribeiro, S.R. de Lazaro, Magnetic, electronic, ferroelectric, structural and topological analysis of AlFeO3, FeAlO3, FeVO3, BiFeO3 and PbFeO3 materials: Theoretical evidences of magnetoelectric coupling, J. Magn. Magn. Mater. 480 (2019) 199–208.
[43] L.H.d.S. Lacerda, S.R. de Lazaro, DFT simulations to clarify the molecular origin of magnetoelectric coupling in R3c materials based on Fe, New J. Chem. 43 (2019) 10610–10617.
[44] L.H.S. Lacerda, S.R. de Lazaro, Multiferroism and magnetic ordering in new $NiBO_3$ (B = Ti, Ge, Zr, Sn, Hf and Pb) materials: A DFT study, J. Magn. Magn. Mater. 465 (2018) 412–420.
[45] L.H.d.S. Lacerda, S.R. de Lazaro, Improvement of multiferroic property and change of magnetic ordering in new $ANiO_3$ (A = Ti, Ge, Zr, Sn, Hf and Pb), Comput. Mater. Sci. 153 (2018) 228–234.
[46] B.G. Janesko, T.M. Henderson, G.E. Scuseria, Screened hybrid density functionals for solid-state chemistry and physics, PCCP 11 (2009) 443–454.
[47] A.D. Becke, Perspective: Fifty years of density-functional theory in chemical physics, J. Chem. Phys. 140 (2014) 318A301–318A320.
[48] I.Y. Zhang, J. Wu, X. Xu, Extending the reliability and applicability of B3LYP, Chem. Commun. 46 (2010) 3057–3070.
[49] A.D. Becke, Density-functional thermochemistry. III. The role of exact exchange, J. Chem. Phys. 98 (1993) 5648–5652.
[50] R. Dovesi, A. Erba, R. Orlando, C.M. Zicovich-Wilson, B. Civalleri, L. Maschio, M. Rérat, S. Casassa, J. Baima, S. Salustro, B. Kirtman, Quantum-mechanical condensed matter simulations with CRYSTAL, Wiley Interdisciplinary Reviews: Computational Molecular, Science 8 (2018) e1360–1336.
[51] R. Dovesi, R. Orlando, B. Civalleri, C. Roetti, V.R. Saunders, C.-M. Zicovich-Wilson, CRYSTAL: a computational tool for the ab initio study of the electronic properties of crystals, Z. Kristallogr. 220 (2005) 571–573.
[52] M.D. Towler, N.L. Allan, N.M. Harrison, V.R. Saunders, W.C. Mackrodt, E. Aprà, Ab initio study of MnO and NiO, Phys. Rev. B 50 (1994) 5041–5054.
[53] F. Cora, A. Patel, N.M. Harrison, C. Roetti, C. Richard, A. Catlow, An ab initio Hartree-Fock study of α-MoO3, J. Mater. Chem. 7 (1997) 959–967.
[54] K. Doll, N.M. Harrison, Chlorine adsorption on the Cu (111) surface, Chem. Phys. Lett. 317 (2000) 282–289.
[55] H.J. Monkhorst, J.D. Pack, Special points for Brillouin-zone integrations, Phys. Rev. B 13 (1976) 5188–5192.
[56] C. Pisani, R. Dovesi, C. Roetti, Hartree-Fock ab initio Treatment of Crystalline Systems, Springer, Berlin Heidelberg, 1988.
[57] R.C. Oliveira, M.M. Teixeira, J.P.C. Costa, M. Penha, E.M. Francisco, J.S. da Silva, M.S. Li, E. Longo, L. Gracia, J. Andrés, α- and β-AgVO3 polymorphs as photoluminescent materials: An example of temperature-driven synthesis, Ceram. Int. 44 (2018) 5939–5944.
[58] G. Botelho, J. Andres, L. Gracia, L.S. Matos, E. Longo, Photoluminescence and Photocatalytic Properties of Ag3PO4 Microcrystals: An Experimental and Theoretical Investigation, ChemPlusChem 81 (2016) 202–212.
[59] R.C. de Oliveira, L. Gracia, M. Assis, M.S. Li, J. Andres, E. Longo, L.S. Cavalcante, Disclosing the electronic structure and optical properties of Ag4V2O7 crystals: experimental and theoretical insights, CrystEngCommCrystEngComm 18 (2016) 6483–6491.
[60] E. Longo, D.P. Volanti, V.M. Longo, L. Gracia, I.C. Nogueira, M.A.P. Almeida, A. N. Pinheiro, M.M. Ferrer, L.S. Cavalcante, J. Andrés, Toward an Understanding of the Growth of Ag Filaments on α-Ag2WO4 and Their Photoluminescent Properties: A Combined Experimental and Theoretical Study, J. Phys. Chem. C 118 (2014) 1229–1239.
[61] R.A.P. Ribeiro, M.C. Oliveira, M.R.D. Bomio, S.R. de Lazaro, J. Andrés, E. Longo, Connecting the surface structure, morphology and photocatalytic activity of Ag2O: An in depth and unified theoretical investigation, Appl. Surf. Sci. 509 (2020), 145321.
[62] H. Ehrenberg, B. Schwarz, H. Weitzel, Magnetic phase diagrams of α-MnMoO4, J. Magn. Magn. Mater. 305 (2006) 57–62.
[63] E.G. Lewars, Computational Chemistry. Introduction to the Theory and Applications of Molecular and Quantum Mechanics, second ed., Springer, Londres, 2011.
[64] M.I. Aroyo, D. Orobengoa, G. de la Flor, E.S. Tasci, J.M. Perez-Mato, H. Wondratschek, Brillouin-zone database on the Bilbao Crystallographic Server, Acta Crystallographica Section A 70 (2014) 126–137.
[65] F. Oba, Y. Kumagai, Design and exploration of semiconductors from first principles: A review of recent advances, Appl. Phys Express 11 (2018), 060101.
[66] C. Freysoldt, B. Grabowski, T. Hickel, J. Neugebauer, G. Kresse, A. Janotti, C. G. Van de Walle, First-principles calculations for point defects in solids, Rev. Mod. Phys. 86 (2014) 253–305.
[67] L.H.S. Lacerda, S.R.d. Lazaro, Ba-doped ZnO Materials: A DFT simulation to investigate the doping effect on ferroelectricity, Quim. Nova 39 (2016) 261–266.
[68] L.H.S. Lacerda, S.R. de Lazaro, A theoretical investigation of the Zn-doping influence on structural and electronic properties of $BaTiO_3$, Solid State Ionics 297 (2016) 36–42.
[69] L.H.S. Lacerda, S.R. de Lazaro, Density Functional Theory investigation of rhombohedral multiferroic oxides for photocatalytic water splitting and organic photodegradation, J. Photochem. Photobiol., A 400 (2020).
[70] Q. Zhou, Y. Liu, W. Ju, Q. Zhang, J. Li, Exploring the effect of dopant (Si, P, S, Ge, Se, and Sb) in arsenene: A DFT study, Phys. Lett. A 384 (2020), 126146.
[71] A. Majorana, R.M. Pidatella, A Finite Difference Scheme Solving the Boltzmann-Poisson System for Semiconductor Devices, J. Comput. Phys. 174 (2001) 649–668.
[72] P.D. Kichambare, R.B. Kharat, Photoelectrochemical studies of MnMoO4 electrodes, Solar Energy Materials 22 (1991) 63–68.
[73] Y.P. Yadava, R.A. Singh, Electrical conduction in manganese molybdate, Mater. Chem. Phys. 17 (1987) 259–272.
[74] H.Y. He, Hydrogen generation from the H2O/H2O2/MnMoO4 system, JOM 63 (2011) 60–62.
[75] D. Yi, F. Hui, Z. Fengjun, F. Youchun, Z. Qicai, Preparation of MnMoO4·XH2O (X=0.9, 1.5) by a Microemulsion Method under Different Manganese Precursors and Analysis of Their Band-gap Energy, Rare Met. Mater. Eng. 46 (2017) 68–72.
[76] F. Namvar, F. Beshkar, M. Salavati-Niasari, Novel microwave-assisted synthesis of leaf-like MnMoO4 nanostructures and investigation of their photocatalytic performance, J. Mater. Sci.: Mater. Electron. 28 (2017) 7962–7968.
[77] V.G. Bessergenev, Y.A. Kovalevskaya, I.E. Paukov, M.A. Starikov, H. Oppermann, W. Reichelt, Thermodynamic properties of MnMoO4 and Mn2Mo3O8, J. Chem. Thermodyn. 24 (1992) 85–98.
[78] J. Yu, P. Zhou, Q. Li, New insight into the enhanced visible-light photocatalytic activities of B-, C- and B/C-doped anatase TiO_2 by first-principles, PCCP 15 (2013) 12040–12047.
[79] P. Zhou, J. Yu, Y. Wang, The new understanding on photocatalytic mechanism of visible-light response NS codoped anatase TiO_2 by first-principles, Appl. Catal. B 142–143 (2013) 45–53.
[80] X. Ma, Y. Dai, M. Guo, B. Huang, The Role of Effective Mass of Carrier in the Photocatalytic Behavior of Silver Halide-Based Ag@AgX (X = Cl, Br, I): A Theoretical Study, ChemPhysChem 13 (2012) 2304–2309.
[81] G.B. Soares, R.A.P. Ribeiro, S.R. de Lazaro, C. Ribeiro, Photoelectrochemical and theoretical investigation of the photocatalytic activity of TiO_2:N, RSC Adv. 6 (2016) 89687–89698.
[82] N. Gao, C. Quan, Y. Ma, Y. Han, Z. Wu, W. Mao, J. Zhang, J. Yang, X.a. Li, W. Huang, Experimental and first principles investigation of the multiferroics $BiFeO_3$ and $Bi_{0.9}Ca_{0.1}FeO_3$: Structure, electronic, optical and magnetic properties, Phys. B 481 (2016) 45–52.
[83] Y. Gu, J. Zhao, W. Zhang, H. Zheng, L. Liu, W. Chen, Structural transformation and multiferroic properties of Sm and Ti co-doped $BiFeO_3$ ceramics with Fe vacancies, Ceram. Int. 43 (2017) 14666–14671.

[84] A. Das, S. De, S. Bandyopadhyay, S. Chatterjee, D. Das, Magnetic, dielectric and magnetoelectric properties of $BiFeO_3$-$CoFe_2O_4$ nanocomposites, J. Alloy. Compd. 697 (2017) 353–360.

[85] T. Murtaza, J. Ali, M.S. Khan, K. Asokan, Structural, electrical and magnetic properties of multiferroic $BiFeO_3$–$SrTiO_3$ composites, J. Mater. Sci.: Mater. Electron. 29 (2018) 2110–2119.

[86] X. Chen, Y. Dai, X. Wang, Methods and mechanism for improvement of photocatalytic activity and stability of Ag3PO4: A review, J. Alloy. Compd. 649 (2015) 910–932.

[87] R.-Z. Zhang, X.-Y. Hu, P. Guo, C.-L. Wang, Thermoelectric transport coefficients of n-doped CaTiO3, SrTiO3 and BaTiO3: A theoretical study, Phys. B 407 (2012) 1114–1118.

[88] A. Dasmahapatra, L.E. Daga, A.J. Karttunen, L. Maschio, S. Casassa, The Key Role of Defects in Thermoelectric Performance of TiMSn(M = Ni, Pd, Pt) Half-Heusler Alloys, J. Phys. Chem. C (2020).

[89] A.J. Cohen, P. Mori-Sanchez, W. Yang, Fractional charge perspective on the band gap in density-functional theory, Phys. Rev. B, Condens. Matter Mater. Phys. 77 (2008), 115123.

[90] C. Yue, X. Lu, J. Zhang, F. Huang, J. Zhu, Ferroelectric surface chemistry: First-principles study of adsorption on the stoichiometric $LiNbO_3$ (0001) surface, Phys. Rev. B 100 (2019), 245432.

[91] K. Doll, CO adsorption on the Pt(111) surface: a comparison of a gradient corrected functional and a hybrid functional, Surf. Sci. 573 (2004) 464–473.

[92] S. Baud, C. Ramseyer, G. Bihlmayer, S. Blügel, C. Barreteau, M.C. Desjonquères, D. Spanjaard, N. Bernstein, Comparative study of ab initio and tight-binding electronic structure calculations applied to platinum surfaces, Phys. Rev. B 70 (2004), 235423.

[93] A. Kahn, Fermi level, work function and vacuum level, Mater. Horiz. 3 (2016) 7–10.

[94] F. Lipsky, L.H.D.S. Lacerda, S.R. de Lazaro, E. Longo, J. Andrés, M.A. San-Miguel, Unraveling the relationship between exposed surfaces and the photocatalytic activity of Ag3PO4: an in-depth theoretical investigation, RSC Adv. 10 (2020) 30640–30649.

[95] O.T. Hofmann, J.-C. Deinert, Y. Xu, P. Rinke, J. Stähler, M. Wolf, M. Scheffler, Large work function reduction by adsorption of a molecule with a negative electron affinity: Pyridine on ZnO($10\bar{1}0$), J. Chem. Phys. 139 (2013), 174701.

[96] D. Jiang, W. Wang, Fundamental Studies on Photocatalytic Structures With Well-Defined Crystal Facets, in: P. Fornasiero, M. Cargnello (Eds.), Studies in Surface Science and Catalysis, Elsevier, 2017, pp. 409–438.

[97] L.C. Hirst, Principles of Solar Energy Conversion, in: A. Sayigh (Ed.), Comprehensive Renewable Energy, Elsevier, Oxford, 2012, pp. 293–313.

[98] J.J. Liu, X.L. Fu, S.F. Chen, Y.F. Zhu, Electronic structure and optical properties of Ag3PO4 photocatalyst calculated by hybrid density functional method, Appl. Phys. Lett. 99 (2011), 191903.

[99] M. Mousavi, A. Habibi-Yangjeh, M. Abitorabi, Fabrication of novel magnetically separable nanocomposites using graphitic carbon nitride, silver phosphate and silver chloride and their applications in photocatalytic removal of different pollutants using visible-light irradiation, J. Colloid Interface Sci. 480 (2016) 218–231.

[100] H. Dong, J. Sun, G. Chen, C. Li, Y. Hu, C. Lv, An advanced Ag-based photocatalyst Ag2Ta4O11 with outstanding activity, durability and universality for removing organic dyes, PCCP 16 (2014) 23915–23921.

[101] D. Katakis, C. Mitsopoulou, E. Vrachnou, Photocatalytic splitting of water: increase in conversion and energy storage efficiency, J. Photochem. Photobiol., A 81 (1994) 103–106.

[102] A. Kushwaha, R.S. Moakhar, G.K.L. Goh, G.K. Dalapati, Morphologically tailored CuO photocathode using aqueous solution technique for enhanced visible light driven water splitting, J. Photochem. Photobiol., A 337 (2017) 54–61.

[103] A. Machín, M. Cotto, J. Duconge, J.C. Arango, C. Morant, S. Pinilla, L. Soto-Vázquez, E. Resto, F. Márquez, Hydrogen production via water splitting using different Au@ZnO catalysts under UV–vis irradiation, J. Photochem. Photobiol., A 353 (2018) 385–394.

[104] A.M. Huerta-Flores, D. Sánchez-Martínez, M. del Rocío Hernández-Romero, M. E. Zarazúa-Morín, L.M. Torres-Martínez, Visible-light-driven BaBiO3 perovskite photocatalysts: Effect of physicochemical properties on the photoactivity towards water splitting and the removal of rhodamine B from aqueous systems, J. Photochem. Photobiol., A 368 (2019) 70–77.

[105] E. HassCaetanoLacerda, F.C. Monteiro, J.R. Kloss, S.T. Fujiwara, Bentonite clay modified with Nb2O5: An efficient and reused photocatalyst for the degradation of reactive textile dye, J. Photochem. Photobiol., A 388 (2020).

[106] S. Nahar, M.R. Hasan, A.A.H. Kadhum, H.A. Hasan, M.F.M. Zain, Photocatalytic degradation of organic pollutants over visible light active plasmonic Ag nanoparticle loaded Ag2SO3 photocatalysts, J. Photochem. Photobiol., A 375 (2019) 191–200.

[107] G.G.D. Toledo, V.H. Toledo, A.J.C. Lanfredi, M. Escote, A. Champi, M.C.C. D. Silva, I.L. Nantes-Cardoso, Promising Nanostructured Materials against Enveloped Virus, Anais da Academia Brasileira de Ciências 92 (2020).

[108] W. He, J. Cai, X. Jiang, J.-J. Yin, Q. Meng, Generation of reactive oxygen species and charge carriers in plasmonic photocatalytic Au@TiO2 nanostructures with enhanced activity, PCCP 20 (2018) 16117–16125.

[109] D. He, A.M. Jones, S. Garg, A.N. Pham, T.D. Waite, Silver Nanoparticle−Reactive Oxygen Species Interactions: Application of a Charging−Discharging Model, J. Phys. Chem. C 115 (2011) 5461–5468.

[110] Y. Seo, K. Park, Y. Hong, E.S. Lee, S.-S. Kim, Y.-T. Jung, H. Park, C. Kwon, Y.-S. Cho, Y.-D. Huh, Reactive-oxygen-species-mediated mechanism for photoinduced antibacterial and antiviral activities of Ag3PO4, J. Anal. Sci. Technol. 11 (2020) 21.

[111] M. Miyauchi, K. Sunada, K. Hashimoto, Antiviral Effect of Visible Light-Sensitive CuxO/TiO2, Photocatalyst 10 (2020) 1093.

[112] C.N. Paiva, M.T. Bozza, Are Reactive Oxygen Species Always Detrimental to Pathogens? Antioxid. Redox Signal. 20 (2013) 1000–1037.

[113] X. Dong, W. Liang, M.J. Meziani, Y.-P. Sun, L. Yang, Carbon Dots as Potent Antimicrobial Agents, Theranostics 10 (2020) 671–686.

[114] D. Olagnier, S. Peri, C. Steel, N. van Montfoort, C. Chiang, V. Beljanski, M. Slifker, Z. He, C.N. Nichols, R. Lin, S. Balachandran, J. Hiscott, Cellular Oxidative Stress Response Controls the Antiviral and Apoptotic Programs in Dengue Virus-Infected Dendritic Cells, PLoS Pathog. 10 (2014), e1004566.

[115] D. Wang, Y. Zhu, X. Wan, X. Zhang, J. Zhang, Colloidal semiconductor nanocrystals for biological photodynamic therapy applications: Recent progress and perspectives, Progr. Natural Sci. Mater. Int. 30 (2020) 443–455.

[116] V.P. Skulachev, Possible role of reactive oxygen species in antiviral defense, Biochemistry (Mosc) 63 (1998) 1438–1440.

[117] D. Wang, L. Zhao, H. Ma, H. Zhang, L.-H. Guo, Quantitative Analysis of Reactive Oxygen Species Photogenerated on Metal Oxide Nanoparticles and Their Bacteria Toxicity: The Role of Superoxide Radicals, Environ. Sci. Technol. 51 (2017) 10137–10145.

[118] A. Sirelkhatim, S. Mahmud, A. Seeni, N.H.M. Kaus, L.C. Ann, S.K.M. Bakhori, H. Hasan, D. Mohamad, Review on Zinc Oxide Nanoparticles: Antibacterial Activity and Toxicity Mechanism, Nano-Micro Lett. 7 (2015) 219–242.

[119] Y. Li, W. Zhang, J. Niu, Y. Chen, Mechanism of Photogenerated Reactive Oxygen Species and Correlation with the Antibacterial Properties of Engineered Metal-Oxide Nanoparticles, ACS Nano 6 (2012) 5164–5173.

[120] J. Picard, R. Cerf, The Wulff Crystal in Ising and Percolation Models: Ecole d'Eté de Probabilités de Saint-Flour XXXIV - 2004, Springer, Berlin Heidelberg, 2006.

[121] G. Wulff, Zur Frage der Geschwindigkeit des Wachstums und der Auflösung der Krystallflagen, Zeitschrift für Krystallographie und Mineralogie 34 (1901) 449–530.

[122] G.D. Barmparis, Z. Lodziana, N. Lopez, I.N. Remediakis, Nanoparticle shapes by using Wulff constructions and first-principles calculations, Beilstein J. Nanotechnol. 6 (2015) 361–368.

[123] J. Andrés, L. Gracia, A.F. Gouveia, M.M. Ferrer, E. Longo, Effects of surface stability on the morphological transformation of metals and metal oxides as investigated by first-principles calculations, Nanotechnology 26 (2015), 405703.

[124] L.D. Marks, L. Peng, Nanoparticle shape, thermodynamics and kinetics, J. Phys.: Condens. Matter 28 (2016), 053001.

[125] H. Wang, Y. Song, J. Zhou, X. Xu, W. Hong, J. Yan, R. Xue, H. Zhao, Y. Liu, J. Gao, High-performance supercapacitor materials based on polypyrrole composites embedded with core-sheath polypyrrole@MnMoO4 nanorods, Electrochim. Acta 212 (2016) 775–783.

[126] G.M. Martins, P.O. Coelho, K.P.F. Siqueira, R.L. Moreira, A. Dias, Investigation of Polymorphism and Vibrational Properties of MnMoO4 Microcrystals Prepared by a Hydrothermal Process, Cryst. Growth Des. 18 (2018) 2474–2485.

[127] G. Harichandran, S. Radha, P. Divya, J. Yesuraj, Facile morphology-controlled synthesis of nanostructured MnMoO4 nanorods as an advance electrode material for supercapacitor application, J. Mater. Sci.: Mater. Electron. 31 (2020) 1646–1653.

[128] J. Xu, Y. Sun, M. Lu, L. Wang, J. Zhang, J. Qian, X. Liu, Fabrication of hierarchical MnMoO4·H2O@MnO2 core-shell nanosheet arrays on nickel foam as an advanced electrode for asymmetric supercapacitors, Chem. Eng. J. 334 (2018) 1466–1476.

[129] L. Wang, L. Yue, X. Zang, H. Zhu, X. Hao, Z. Leng, X. Liu, S. Chen, Synthesis of 3D α-MnMoO4 hierarchical architectures for high-performance supercapacitor applications, CrystEngCommCrystEngComm 18 (2016) 9286–9291.

[130] S.B. Patil, B. Kishore, M.K. Nagaraj, N. Ganganagappa, U. Velu, Mesoporous MnMoO4 Nanorods for Enhanced Electrochemical Performance, ChemistrySelect 3 (2018) 7490–7495.

[131] F. Nti, D.A. Anang, J.I. Han, Facile room temperature synthesis and application of MnMoO4·0.9H2O as supercapacitor electrode material, Mater. Lett. 217 (2018) 146–150.